ELSEVIER

Chemical Physics 197 (1995) 259–275

Chemical Physics

# Effects of applied electric fields on the quantum yields for the initial electron transfer steps in bacterial photosynthesis. II. Dynamic Stark effect

Kaiqin Lao, Stefan Franzen, Martin Steffen, David Lambright, Robert Stanley, Steven G. Boxer

*Department of Chemistry, Stanford University, Stanford, CA 94305-5080, USA*

Received 25 October 1994

**Abstract**

The quantum yield of the initial charge separation steps in bacterial photosynthetic reaction centers has been shown to be reduced in an applied electric field [Part I, Lao et al., J. Phys. Chem. 97 (1993) 13165]. The mechanism of this quantum yield failure is examined further by measuring the orientations of the subpopulations which return to the ground state in an electric field. Information on the orientations of these subpopulations can be obtained by measuring the Stark effect spectrum of the transient population, the dynamic Stark spectrum, whose lineshape is sensitive to orientation. This is a generally useful method, whose application is developed for general cases. It is shown that considerably more information on orientational subpopulations can be obtained than by conventional photoselection or dichroism methods. In the case of reaction center quantum yield failure, the dynamic Stark spectrum is analyzed to extract information on the absolute orientations of electric dipoles which lead to quantum yield failure. A numerical procedure using the maximum entropy method is developed to map out the most unbiased orientation distribution function from the dynamic Stark spectrum. The distribution of the transient orientational subpopulation depends on the magnitude of the interaction between the applied field and the transient dipole moment(s) associated with the electron transfer intermediate(s) responsible for quantum yield failure. The resulting orientation distribution function suggests that at least two electric-field-dependent mechanisms are important. Based on the X-ray structure of the reaction center, the results are analyzed in terms of contributions from charge-separated states involving internal charge separation within the special pair ($P^+P^-$), the monomeric bacteriochlorophyll ($P^+B^-$) and bacteriopheophytin ($P^+H^-$), each of which can provide field-sensitive shunts to the ground state. Possible relationships with the dynamics of mutants which affect the redox potential of participants in electron transfer are discussed.

## 1. Introduction

The quantum yield for charge separation in photosynthetic reaction centers (RCs) is remarkably high, approaching unity [1]. A reaction scheme illustrating the states that are relevant to the experiments discussed in the following is given in Fig. 1. In Part I of this series [2], it was demonstrated that the application of an external

0301-0104/95/$09.50 
*SSDI* 0301-0104(95)00090-9

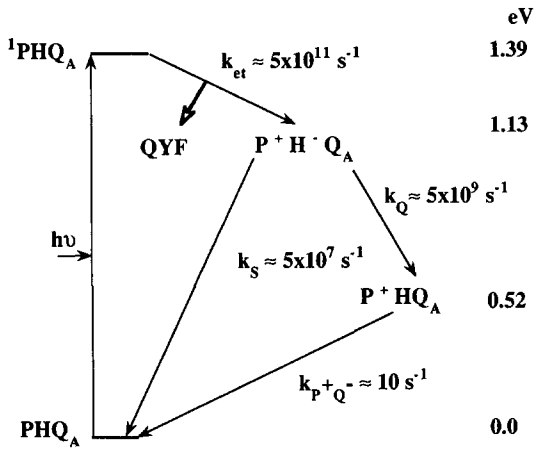


Fig. 1. Approximate kinetics and energetics of the initial charge separation steps in *Rb. sphaeroides* RCs. The kinetics are for low temperature, whereas the energetics are typically obtained at room temperature.

electric field causes a substantial fraction of excited RCs to return to the ground state and reduces the quantum yield for further charge separation, a result independently found by Ogrodnik et al. [3]. In our work, the origin of the quantum yield failure (QYF) was examined by preparing RCs in different initial conditions to determine the role of various intermediates [2,4]. It was concluded that QYF occurs at an early step, illustrated schematically in Fig. 1. An analysis of the origin of QYF is not only interesting from the perspective of understanding the mechanism of the charge separation and recombination reactions in isolated RCs, but may also be physiologically important as a mechanism of regulation of charge separation in response to transmembrane potentials.

The analysis of electric field effects makes the basic assumption that the electric field exerts its effect by interacting with states of the system which have electric dipole moments. Given the experimental results in Part I, the three-dimensional structure of the RC [5], and earlier work from our group [6–8] and other labs [3], we are led to focus on three states: (i) dipolar excited states of the special pair, denoted $P^+P^-$ (e.g. charge transfer states); (ii) the hypothetical intermediate $P^+B^-$, where B is a monomeric bacteriochlorophyll, whose intermediacy in the absence of an electric field is controversial [9], but which may become involved when an electric field is present even if it is not directly populated in the absence of a field; and (iii) the relatively well-characterized intermediate $P^+H^-$. A role can also be imagined for states involving the non-functional M- or B-side redox components or for unrelaxed configurations of the charge-separated intermediates [2]. The purpose of this paper is to develop an experimental method which can provide further information on which intermediate state(s) is responsible for QYF.

For reactive systems, it is possible that some electric-field-dependent process, such as electron transfer, competes with absorption or emission. Because the field interacts with electric dipoles that are created or consumed by an electron transfer, and the electron transfer rate is expected to depend on the driving force, the rate depends on the orientation of these dipoles in an applied electric field [6–8]. Thus, for an initially isotropic sample, in an applied electric field the concentrations of different orientational subpopulations will be different at different times, and the Stark effect spectral lineshape will be different than for an isotropic sample. We call this time-dependent Stark spectrum of a sample undergoing electric-field-dependent chemistry the dynamic Stark effect spectrum. The principle of the approach presented here is related to the effect of an applied electric field on the steady-state fluorescence polarization and lineshape for a non-oriented sample when an electric field dependent process competes with emission. This was developed earlier as a general method with a specific analysis of parameters relevant to RCs [10].

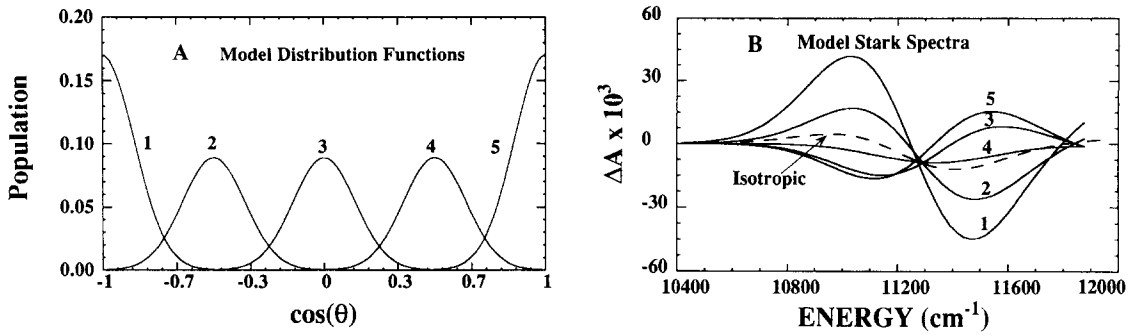


Fig. 2. The effect of uniaxial orientation on the absorption Stark effect spectrum. (A) Five Gaussian orientational distribution functions with same area and width centered at positions $\cos(\theta) = -1.0, -0.5, 0.0, 0.5, 1.0$, where $\theta$ is the angle between the difference dipole $\Delta\boldsymbol{\mu}_A$ and the external field $F$. (B) Stark spectra corresponding to the distribution functions in (A). The dashed line is the Stark spectrum that would result from an isotropic distribution for comparison. In order to be comparable with the data discussed in this paper, parameters relevant to the P absorption band were chosen by fitting the Stark spectrum of RCs in an isotropic sample by using Eq. (21), and using the lineshape function from the absorption spectrum ( $\chi = 56°$, $F = 1.53$ MV/cm).

For a non-oriented, immobilized sample where a change in dipole moment between the ground and excited state, $\Delta\boldsymbol{\mu}_A = \boldsymbol{\mu}_e - \boldsymbol{\mu}_g$, dominates other contributions such as the change in polarizability, hyperpolarizability, etc., the conventional absorption Stark effect spectrum results from interactions between the applied electric field, $\boldsymbol{F}_{ext}$, and $\Delta\boldsymbol{\mu}_A$: $\Delta U = -\Delta\boldsymbol{\mu}_A \cdot \boldsymbol{F}_{ext}$, where $\Delta U$ is the interaction energy. Because all orientations of $\Delta\boldsymbol{\mu}$ are present, the zero-field transition energy is shifted both to higher and lower energy. The difference absorption, $\Delta A$, between this broadened lineshape and the lineshape in the absence of an electric field has the shape of the second derivative of the absorption spectrum, as long as $\Delta U$ is smaller than the inhomogeneous linewidth. If the sample were completely or partially oriented with respect to the applied field, the lineshape would be different in a completely predictable way. This is illustrated in Fig. 2, where a series of anisotropic distributions of $\Delta\boldsymbol{\mu}_A$, characterized by the angle $\theta$ between $\Delta\boldsymbol{\mu}_A$ and $\boldsymbol{F}_{ext}$ (Panel A), leads to a series of very different Stark effect lineshapes (Panel B). It is evident from this figure that were the sample uniaxially oriented by some physical means (e.g. a single crystal or by attachment to a surface) or if some process dynamically produced uniaxial orientation, then the measured Stark effect lineshape provides a direct approach to characterizing the anisotropic distribution, essentially allowing one to go from experimental information as in Panel B to the distribution in Panel A. Note that a biaxial distribution of orientations, such as that produced by photoselection, contains much less information.

The QYF process(es) studied in this paper is an example of an electric-field-dependent mechanism which repopulates the ground state of P by an unknown route(s). The simplest version of the experiment is to measure the induced polarization of the absorption of the subpopulation of P which is formed by the QYF process, because this transient subpopulation is not isotropic. In principle, further information is available by analyzing the dynamic Stark lineshape of ground state P reformed by QYF, as illustrated schematically in Fig. 2. The observable dynamic Stark effect spectrum does not give the orientation of the dipoles responsible for QYF directly in molecular terms, rather the data must be analyzed in terms of the direction of the difference dipole between the electronic ground and excited states ($\Delta\boldsymbol{\mu}_A$) as well as the transition dipole moment used to spectroscopically probe the dynamic Stark spectrum. To the extent that accurate information is available on the direction of the transition dipole moment and $\Delta\boldsymbol{\mu}_A$ relative to the molecular axis, the data can provide information on the direction of dipoles, and thus on the intermediate states responsible for QYF by use of the RC crystal structure.

## 2. Materials and methods

### 2.1. Materials

The experimental apparatus and sample preparation were described in detail in Part I [2]. Quinone ($Q_A$) containing RCs from *Rb. sphaeroides* R-26 in poly(vinylalcohol) thin films were used in all experiments. The probe beam (bandwidth 4.5 nm) was passed through a Glan–Thompson polarizer, which has an extinction of greater than $10^4$. The probe light enters through an indium–tin-oxide electrode, passes through the sample, is reflected off an aluminium electrode and is focused onto a silicon photodiode detector. Scattered laser light was blocked by long pass colored glass filters placed in front of the detector. The incident direction of the probe light was set at Brewster's angle (57°) in order to reduce the reflection of the light from the glass window of the refrigerator and the glass substrate of the sample. The intensity of the probe light was less than 10 $\mu W/cm^2$ (cf. Ref. [11]).

The external electric field was generated by a Stanford Research Instruments DG535 digital delay pulse generator whose output was amplified by a TREK 10/10 high voltage amplifier, which is capable of applying up to 1000 V with a rise time of 20 μs. The experimental angle, $\chi$, between the electric vector of the probe light and the applied field direction is equal to 56°. The field was turned on 30 μs before the 532 nm laser pulse and was turned off 170 μs after the laser excitation, thus the field is at its full voltage during sample excitation and charge separation to form $P^+Q_A^-$ (see Fig. 1). Due to the slew rate of the applied field (ca. 250 V/μs) which is determined by the intrinsic properties of the power supply and the electrode resistance and the sample capacitance, the field reaches its maximum after the field is turned on for about 20 μs. Thus, only data points from 10 to 0 μs before the 532 nm excitation flash were summed to obtain the static Stark spectra (see below). Since some of the 532 nm scattered light passes through the colored glass filters, there are sharp peaks at time zero and the fast decay between 0 and 10 μs which is due to the limiting time response of our detector (ca. 2 μs). This artifact can be removed from the data by subtraction of a decay trace measured at 960 nm where the RC does not absorb.

In order to obtain spectra, the probe light wavelength was varied from 820 to 960 nm in 2 nm increments selected in a random order by the computer. The transient signals were digitized with a Tektronix digital oscilloscope (model DSA602). Transient signals were converted from transmission changes to $\Delta A(\nu, t)$ according to

$$\Delta A(\nu, t) = -\log_{10}[I(\nu, t)/I_{\text{base}}(\nu)],$$

where $I_{\text{base}}(\nu)$ is the transmission intensity at probe frequency $\nu$ prior to the application of the field and the excitation pulse. At a given $\nu$, data were first collected with the field turned on prior to the excitation pulse for 256 laser shots, then the field was turned off, and finally the field was turned on after the laser flash. Typical data collection times were 12 h per complete data set at a given field. The magnitude of the bleach at the end of data collection was unchanged from that at the beginning. The dynamic Stark experiments were performed at applied fields ranging from 1 to 1.7 MV/cm (see Ref. [4] for further details on proper methods for field calibration). Additionally, $P^+Q_A^-$ quantum yield failure was measured at a single wavelength (875 nm) at multiple fields ranging from 0.2 to 1.7 MV/cm with the electric vector of the probe light such that $\chi = 56°$ or 90° (perpendicular to the field direction). Details of the measurement of QYF can be found in Part I [2]. The experiments were performed on samples from two independent preparations.

### 2.2. Methods

In an applied field, there are many processes which can contribute to the transient absorbance change. To obtain the absorption change due to the dynamic Stark effect for the P band in RCs, absorption changes due to the bleach of the P absorption band, and the static Stark effect on the non-excited subpopulation were taken into

account by using three different experimental configurations. *Case 1*: kinetic traces are taken with zero applied field to determine the bleach of P (bleaching). *Case 2*: the field is turned on prior to the excitation flash, and the signal reflects changes due to both the dynamic and static Stark contributions (pre-flash). The signal is evaluated from 60 to 170 μs so that $P^+Q_A^-$ recombination has not yet occurred (its decay rate is about 200 ms). *Case 3*: kinetic traces are taken with the field turned on after the excitation pulse in order to determine the contribution for the static Stark spectrum due to the non-excited subpopulation (post-flash), so that it can be subtracted from the signal obtained in Case 2. In this third experimental configuration no quantum yield failure is observed at low temperature consistent with previous reports of the electric field effect on $P^+Q^-$ recombination at low temperature [12].

*Case 1. Zero electric field – bleaching*

The change of the extinction coefficient $\Delta\varepsilon(\nu, t, F = 0)$ is a consequence of the time-dependent bleach of the P band at zero field,

$$\Delta\varepsilon(\nu, t, F = 0) = \eta\langle\Delta\varepsilon_e(\nu, t, F = 0)\rangle, \tag{1}$$

where $\nu$ is the frequency of the absorbed photons, $F$ is the externally applied electric field which is zero in this case, $\eta$ is the fraction of molecules which are initially excited into their electronic excited state (isotropic excitation) at zero applied field, and $\Delta\varepsilon_e(\nu, t, F = 0)$ is the change of the extinction coefficient for the molecules which are in their electronic excited state. Orientation averaging is indicated by $\langle\ \rangle$.

*Case 2. Electric field turned on prior to excitation – pre-flash*

When the electric field is turned on prior to the excitation pulse, the time-dependent change in the extinction coefficient $\Delta\varepsilon(\nu, t, F)$ is given by

$$\begin{aligned}\Delta\varepsilon(\nu, t, F) = {} & \langle(1 - \eta(F))\Delta\varepsilon_g(\nu, F)\rangle \\ & + \langle\eta(F)\left(\sum_{i=1}^{n}\Phi_i(F)\left(1 - \exp[-k_i(F)t]\right)\right)\Delta\varepsilon_g(\nu, F)\rangle \\ & + \langle\eta(F)\left(\sum_{i=1}^{n}\Phi_i(F)\exp[-k_i(F)t]\right)\Delta\varepsilon_e(\nu, F)\rangle.\end{aligned} \tag{2}$$

The first term describes the Stark effect for those molecules which were unexcited and remain in the ground state throughout; the second term describes the Stark effect for RCs which have returned to the ground state at the time of the measurement; and the third term describes the Stark effect for RCs in the excited state at time $t$. $\eta(F)$ is the fraction of molecules which are initially excited into their electronic excited state and can be a function of the applied field. $\Delta\varepsilon_g(\nu, F)$ and $\Delta\varepsilon_e(\nu, F)$ are the field-induced changes of the extinction coefficients of the molecules which are in their electronic ground state and excited state, respectively. $\Phi_i(F)$ is the fraction of molecules which return to the ground state via the $i$th pathway, $k_i(F)$ is the associated field-dependent decay rate constant, and $\Sigma\Phi_i(F) = 1$. For the case of the RC, there are at least three processes: $\Phi_1(F)$ is the fraction of excited molecules which undergo rapid, field-induced decay to the ground state due to QYF of the primary step; $\Phi_2(F)$ is the fraction which decays to the ground state due to an activated recombination pathway of $P^+Q_A^-$ through the $P^+H^-$ state [12]; and $\Phi_3(F)$ is the fraction of RCs which recombines from $P^+Q_A^-$ to the ground state. The time scales of these three processes are approximately ps, μs and ms, respectively (see Fig. 1).

In Part I, it has been shown that the field dependence of the relative quantum yield of the states $P^+H^-$, $P^+Q_A^-$ and $^3P$ are essentially identical [2]. Therefore all quantum yield failure processes occur on a time scale shorter than the formation of the $P^+Q_A^-$ state ($< 200$ ps). The dynamic Stark spectra discussed below were measured on the μs time scale. Thus, the term $\exp[-k_1(F)t]$ will be zero at the time of the measurement. Since

the recombination rate of the $P^+Q_A^-$ state is $\sim 50\ s^{-1}$ [12], the term $\exp[-k_3(F)t]$ is approximately unity at the time of the measurement. Using these approximations, Eq. (2) reduces to

$$\begin{aligned}\Delta\varepsilon(\nu, t, F) = &\langle(1-\eta(F))\Delta\varepsilon_g(\nu, F)\rangle \\ &+ \langle\eta(F)\Phi_1(F)\Delta\varepsilon_g(\nu, F)\rangle + \langle\eta(F)\Phi_2(F)\{1-\exp[-k_2(F)t]\}\Delta\varepsilon_g(\nu, F)\rangle \\ &+ \langle\eta(F)\Phi_2(F)\exp[-k_2(F)t]\Delta\varepsilon_e(\nu, F)\rangle + \langle\eta(F)\Phi_3(F)\Delta\varepsilon_e(\nu, F)\rangle. \qquad (3)\end{aligned}$$

In Eq. (3), the first term is again the Stark effect of those molecules which remain in the ground state. The second term is the Stark effect of those molecules which have returned to the ground state due to the field-induced quantum yield failure at an early step. The third term describes the Stark effect of those molecules which have returned to the ground state through activated recombination of $P^+Q_A^-$. The fourth and fifth terms describe the Stark effect of RCs that are in the $P^+Q_A^-$ state at the time of the dynamic Stark effect measurement.

*Case 3. Electric field turned on after the excitation pulse – post-flash*

If the field is turned on after the laser flash and initial charge separation steps, there is no QYF. The change of the extinction coefficient $\Delta\varepsilon'(\nu, t, F)$ is given by

$$\begin{aligned}\Delta\varepsilon'(\nu, t, F) = &(1-\eta)\langle\Delta\varepsilon_g(\nu, F)\rangle + \eta\langle\Phi_2'(F)\{1-\exp[-k_2(F)t]\Delta\varepsilon_g(\nu, F)\rangle \\ &+ \eta\langle\Phi_2'(F)\exp[-k_2(F)t]\Delta\varepsilon_e(\nu, F)\rangle + \eta\langle\Phi_3(F)\Delta\varepsilon_e(\nu, F)\rangle. \qquad (4)\end{aligned}$$

The terms here are defined as in Eq. (3), except that now $\Phi_2'(F) + \Phi_3(F) = 1$, with $\Phi_2'(F)$ not equal to $\Phi_2(F)$ in general. Typically, $\Phi_2'(F) \geqslant \Phi_2(F)$.

Eqs. (2)–(4) are the general expressions for transient absorption changes in an applied electric field, assuming quantum yield failure occurs quickly, as is appropriate for the RC. In the following, the equations will be further simplified for the case of RC experiments done at low temperature (60 K). At 60 K and an applied field less than 2 MV/cm, it has been shown that field-induced activated recombination from the $P^+Q_A^-$ state is negligible, hence $\Phi_2(F)$ and $\Phi_2'(F)$ are approximately zero [12]. Furthermore, the absorption Stark effect at 532 nm (the excitation wavelength) is very small [13], so $\eta$ can be treated as a constant. Eqs. (3) and (4) can then be simplified to:

$$\begin{aligned}\Delta\varepsilon(\nu, t, F) = &(1-\eta)\langle\Delta\varepsilon_g(\nu, F)\rangle + \eta\langle\Phi_1(F)\Delta\varepsilon_g(\nu, F)\rangle \\ &+ \eta\langle\Delta\varepsilon_e(\nu, F)\rangle - \eta\langle\Phi_1(F)\Delta\varepsilon_e(\nu, F)\rangle, \qquad (5)\end{aligned}$$

$$\Delta\varepsilon'(\nu, t, F) = (1-\eta)\langle\Delta\varepsilon_g(\nu, F)\rangle + \eta\langle\Delta\varepsilon_e(\nu, F)\rangle. \qquad (6)$$

The dynamic Stark effect of those molecules that have undergone QYF is contained in the second term of Eq. (5). The first, third and fourth terms in Eq. 5 can be evaluated from cases 1 and 2. In addition, it has been shown that the bleach of the P band when RCs are excited with 532 nm light at high photon fluence ($> 1.5\ mJ/cm^2$) corresponds approximately to an isotropic distribution of RCs [14]. We can then write

$$\Delta\varepsilon_e(\nu, F) = \Delta\varepsilon_e(\nu, F=0). \qquad (7)$$

The dynamic Stark spectrum, represented by $\Delta\varepsilon^{DSS}(\nu, t, F)$, can be calculated using the results of Eqs. (5)–(7):

$$\begin{aligned}\Delta\varepsilon^{DSS}(\nu, t, F) = &\eta\langle\Phi_1(F)\Delta\varepsilon_g(\nu, F)\rangle \\ = &\Delta\varepsilon(\nu, t, F) - [\Delta\varepsilon'(\nu, t, F) - \Delta\varepsilon(\nu, t, F=0)] \\ &- \Delta\varepsilon(\nu, t, F=0) + \eta\langle\Phi_1(F)\Delta\varepsilon_e(\nu, t, F=0)\rangle. \qquad (8)\end{aligned}$$

Eq. (8) is complicated by the fact that the population that undergoes QYF is not isotropic in the presence of the applied field. The first term in Eq. (8) is the experimental result of case 2, which contains the lineshape changes

due to the dynamic Stark effect, the static Stark effect, and the anisotropic bleach. The second term combines the experimental results from cases 3 and 1, and is the static Stark effect for the non-excited subpopulation. The third term is a result from case 1, which subtracts the isotropic bleach. The fourth term adds back the anisotropic absorption change due to the populations which undergo QYF (see Eq. (22) in the methods of analysis Section for further development).

## 3. Results

The relative quantum yield of the $P^+Q_A^-$ state as a function of applied field and the angle $\chi$ between the electric vector of the probe light and the direction of the applied field are shown in Fig. 3. The data for the two angles are nearly identical within the signal to noise. This result indicates that the angle between the $Q_y$ transition dipole moment of the special pair and the difference dipole moment(s) responsible for QYF is nearly the magic angle (54.7°). The solid and the dashed lines are the model fitting curves which will be addressed below in the method of analysis section.

The transient absorption at 870 nm for the three different experimental configurations presented in the experimental section are plotted in Fig. 4A, along with the time dependence of the applied field in Fig. 4B. The sharp features between 0 to 10 μs due to the 532 nm scatted light and the limiting time response of our detector are removed from the decay traces (see Section 2.2.). By collecting such decays at multiple wavelengths within the $Q_y$ transition of P, spectra of the absorption changes for the corresponding conditions of field application were obtained as shown in Fig. 5. In the pre-flash configuration, the decrease in absorption at 870 nm which is observed prior the laser flash is due to the static Stark effect ($\Delta A$ for this contribution can be either positive or negative depending on the probe wavelength as shown in the full spectra in Figs. 5 and 6). The value of $\Delta A$ was averaged between 10 μs before the excitation (by which time the field has slewed to its full value) and time zero as a function of wavelength to give the static Stark spectrum (Fig. 5). The absorbance changes in the pre-flash configuration measured in the 60–170 μs time window after the excitation flash are the sum of the bleaching of P, dynamic and static Stark effects. The absorbance changes in the post-flash configuration reflect the contributions from the bleaching and static Stark effect. Due to the overshoot and slew rate of the applied field, the data prior to 60 μs in the post-flash configuration are not used. The static Stark lineshapes at several applied dc fields are shown in Fig. 6A and are found to be identical with that obtained using conventional ac field modulation and lockin detection techniques [15]. As described in the next section, Eq. (8) and the transient

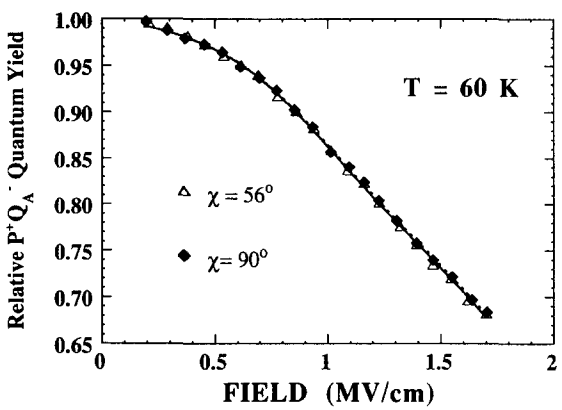


Fig. 3. The relative quantum yield of $P^+ Q_A^-$ formation as a function of the applied electric field at 60 K in a PVA film. The solid line is the model fit based on Eq. (19d) for the experimental angle $\chi = 56°$ (triangles) and the dotted line is the model fit for the experimental angle $\chi = 90°$ (solid diamonds). The experimental errors are less than the size of symbols.

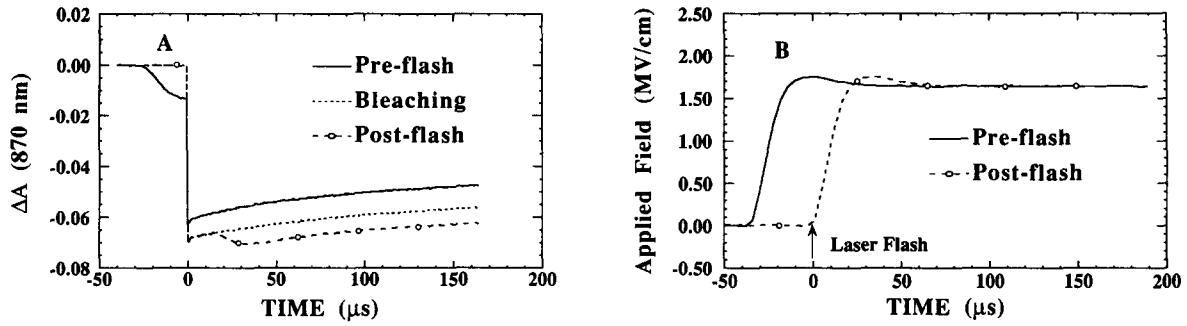


Fig. 4. (A) Kinetic traces for three experimental configurations described in Section 2.2 (probe at 870 nm, $T = 60$ K): field turned off (bleaching); field turned on prior the laser flash (pre-flash); and field turned on 1 μs after the laser flash (post-flash). The feature from 0 to 60 μs on the post-flash curve is due to the overshoot of the applied field. (B) Kinetic traces with the applied electric field turned on 40 μs prior to the laser flash (solid line) and turned on 1 μs after the laser flash (dotted-circles lines).

signals obtained using the three experimental configurations were used to obtain the dynamic Stark spectrum (Fig. 6B).

The dynamic Stark spectra (Fig. 6B) at several applied fields are quite different from the corresponding isotropic Stark spectra (Fig. 6A). Before embarking on a detailed analysis in the next Section, a few comments may be useful. The obvious difference between the dynamic Stark and the isotropic Stark spectra is that field-independent crossing points are no longer isobestic points. The reason is that, in contrast to the static Stark spectrum, the dynamic Stark spectrum is no longer quadratically dependent on the applied field because it arises from a transient anisotropic distribution. Inspection shows that the isobestic point in the static Stark spectrum, located at around 11000 $cm^{-1}$, shifts approximately 50 $cm^{-1}$ to the red and is below the $\Delta A = 0$ line in the dynamic Stark spectra. Since the line shapes of the static and dynamic Stark spectra are not very different from each other,it is reasonable to have some crossing points in the dynamic Stark spectra near the isobestic point of the static Stark spectrum. Without any quantitative analysis, it is observed that the existence of a field-indepen-

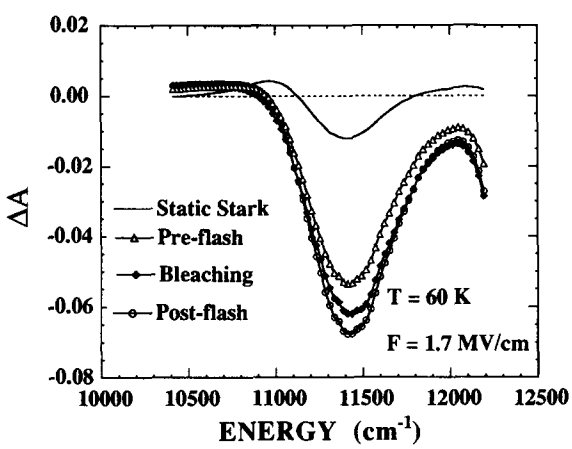


Fig. 5. Spectra of the absorption changes for the three experimental configurations described in Section 2.2. (1) Pre-flash: averaged absorption changes of the kinetic signals between 10 μs before the excitation and time zero as a function of wavelength gives the static or isotropic Stark spectrum (solid line), while the averaged absorption change of the kinetic signals between 60 and 170 μs after the excitation gives the pre-flash spectrum (triangles); (2) Bleaching: the averaged absorption changes of the kinetic signals between 60 and 170 μs after the excitation as a function of wavelength gives the bleaching spectrum (diamonds); (3) Post-flash: the averaged absorption of the kinetic signals between 60 and 170 μs after excitation as a function of wavelength gives the post-flash spectrum (triangles).

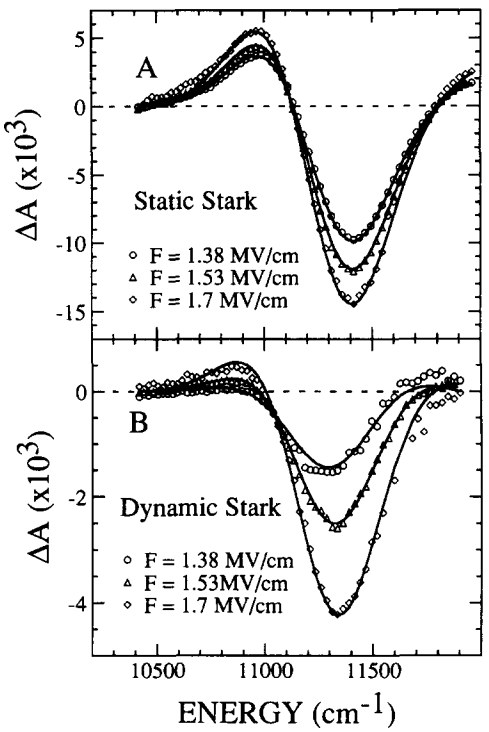


Fig. 6. The isotropic and dynamic Stark spectra of the special pair at three different applied electric fields for the experimental angle $\chi = 56°$ at 60 K. (A) The isotropic Stark spectra obtained from the averaged absorption changes of the kinetic signal between 10 μs before excitation and time zero in the pre-flash experimental configuration fit by Eq. (21) with the isotropic distribution function ($g[\cos(\theta) = 1$, solid lines); and (B) the dynamic Stark spectra of P obtained by using Eqs. (8) and (21) to fit the averaged absorption changes of the kinetic signal between 60 and 170 μs after excitation as a function of wavelength for three experimental configurations.

dent crossing point near 11000 $cm^{-1}$ in the dynamic Stark spectra in Fig. 6B indicates similar distribution functions (cf. Fig. 2A) for RCs which undergo QYF in the field range 1.3–1.7 MV/cm. In general, there is no reason to expect field-independent points in the Stark spectrum of an anisotropic sample.

A further qualitative observation is that the minima of the dynamic Stark spectra shift to higher energy (i.e. close to the field independent minimum of the isotropic Stark spectrum) as the field is increased. At $F = 1.38$ MV/cm, the shift is 103 $cm^{-1}$, while at $F = 1.7$ MV/cm, the shift is only 52 $cm^{-1}$. The smaller red shift at higher applied fields is consistent with the limiting case in which all of the RCs undergo QYF due to the high applied field. In the limit of $F$ being extremely high, one would expect the dynamic Stark spectrum will have same lineshape as the static Stark spectrum, as all excited RCs return to the ground state by quantum yield failure.

## 4. Method of analysis

### *4.1. Model for the dynamic Stark effect*

The extinction coefficient $\varepsilon(\nu, F)$ as a function of frequency $\nu$ can be written as [16]

$$\varepsilon(\nu, F) = K\nu\langle[e \cdot p]^2 S(\nu, F)\rangle, \tag{9}$$

where $K$ is a proportionality constant, $\boldsymbol{e}$ is the electric vector of a polarized probe beam, $\boldsymbol{p}$ is the transition dipole moment, and $S(\nu, F)$ is the lineshape function for the absorption band. The transition dipole moment in an electric field can be expressed to second order as

$$\boldsymbol{p} = \boldsymbol{p}_0 + \mathbf{A} \cdot \boldsymbol{F} + \mathbf{B} \cdot \boldsymbol{F}^2, \tag{10}$$

where $\boldsymbol{p}_0$ is the static transition dipole moment, $\mathbf{A}$ is the transition polarizability tensor, and $\mathbf{B}$ is the transition hyperpolarizability tensor. Typically, the lineshape function $S(\nu, F)$ can be represented by a sum of Gaussians:

$$S(\nu, F) = \sum_i^N \exp\left[-(\nu - \nu_i - \Delta\nu)^2/\omega_i^2\right], \tag{11}$$

where $\omega_i$ is the width of the Gaussian function and $N$ is the number of Gaussian functions. The frequency shift $\Delta\nu$ due to an applied electric field is given by

$$\Delta\nu = -\Delta\boldsymbol{\mu}_A \cdot \boldsymbol{F} - \boldsymbol{F} \cdot \Delta\boldsymbol{\alpha} \cdot \boldsymbol{F}/2, \tag{12}$$

where $\Delta\mu_A$ and $\Delta\boldsymbol{\alpha}$ are the difference dipole moment and the difference polarizability between the excited state and the ground state, respectively. Since the magnitude of $\boldsymbol{F} \cdot \Delta\boldsymbol{\alpha} \cdot \boldsymbol{F}/2$ is small relative to $\Delta\boldsymbol{\mu}_A \cdot \boldsymbol{F}$ for experimentally obtainable fields and even for large values of $\Delta\boldsymbol{\alpha}$, $S(\nu, F)$ can be expanded in a Taylor series in terms up to $F^2$:

$$S(\nu, F) = \sum_i^N \left[1 - \boldsymbol{F} \cdot \Delta\boldsymbol{\alpha} \cdot \boldsymbol{F}(\nu - \nu_i)/\omega_i^2\right] \exp\left[-(\nu - \nu_i + \Delta\boldsymbol{\mu}_A \cdot \boldsymbol{F})^2/\omega_i^2\right]. \tag{13}$$

The dynamic Stark term $\Delta\varepsilon^{DSS}(\nu, F)$ has the following form:

$$\Delta\varepsilon^{DSS}(\nu, F) = K\nu\left\{\langle\eta\Phi_1(F)\left[(\boldsymbol{e} \cdot \boldsymbol{p})^2 S(\nu, F) - (\boldsymbol{e} \cdot \boldsymbol{p}_0)^2 S(\nu, F = 0)\right]\rangle\right\}. \tag{14}$$

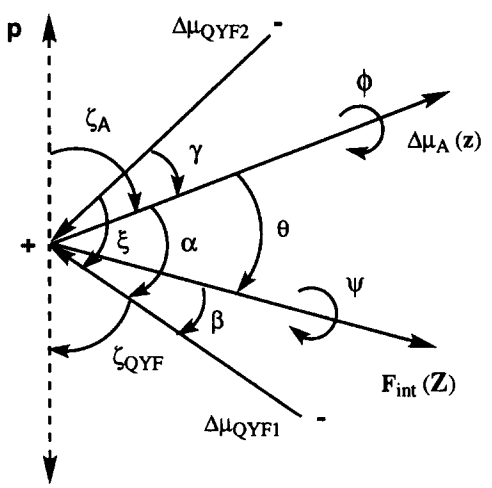


Fig. 7. Coordinate system used in the analysis of the dynamic Stark spectra. The external applied field $F$ is chosen to lie along the $Z$ axis in the laboratory frame and the difference dipole moment $\Delta\boldsymbol{\mu}_A$ lies along the $z$ axis in the molecular frame, with $\theta$ the angle between $\Delta\boldsymbol{\mu}_A$ and $F$. $\zeta_A$ is the angle in the molecular frame between the transition dipole moment $\boldsymbol{p}$ and $\Delta\boldsymbol{\mu}_A$. $\alpha$ is the angle between $\Delta\boldsymbol{\mu}_{QYF1}$ and $\Delta\boldsymbol{\mu}_A$ ($\Delta\boldsymbol{\mu}_{QYF1}$ in the $yz$ plane); $\gamma$ is the angle between $\Delta\boldsymbol{\mu}_{QYF2}$ and $\Delta\boldsymbol{\mu}_A$; $\beta$ is the angle between $\Delta\boldsymbol{\mu}_{QYF1}$ and $F$; $\xi$ is the angle between $\Delta\boldsymbol{\mu}_{QYF1}$ and $\Delta\boldsymbol{\mu}_{QYF2}$. $\zeta_{QYF}$ is the angle between the transition dipole moment $\boldsymbol{p}$ and $\Delta\boldsymbol{\mu}_{QYF1}$. Note: the direction of $\Delta\boldsymbol{\mu}_{QYF}$ described in Eq. (19d) is assumed to be the same as $\Delta\boldsymbol{\mu}_{QYF1}$.

To avoid double numerical integration, we choose our reference frame such that $\Delta\boldsymbol{\mu}_A$ lies along the $z$ axis in the molecular frame, and $\boldsymbol{F}$ lies along the $Z$ axis in the laboratory frame as shown in Fig. 7. Keeping terms up to $F^2$, the following equations are obtained:

$$\Delta\boldsymbol{\mu}_A \cdot \boldsymbol{F} = |\Delta\boldsymbol{\mu}_A||\boldsymbol{F}|\cos(\theta), \tag{15a}$$

$$(\boldsymbol{e}\cdot\boldsymbol{p})^2 = (\boldsymbol{e}_{\parallel}\cdot\boldsymbol{p})^2\cos^2(\chi) + (\boldsymbol{e}_{\perp}\cdot\boldsymbol{p})^2\sin^2(\chi), \tag{15b}$$

$$(\boldsymbol{e}_{\parallel}\cdot\boldsymbol{p})^2 = \sum p_i p_j l_i l_j + F\sum p_i A_{jk} l_i l_j l_k + F^2\sum A_{ik}A_{jl} l_i l_j l_k l_l + F^2\sum p_i B_{jkl} l_i l_j l_k l_l, \tag{15c}$$

$$(\boldsymbol{e}_{\perp}\cdot\boldsymbol{p})^2 = \sum p_i p_j l'_i l'_j + F\sum p_i A_{jk} l'_i l'_j l_k + F^2\sum A_{ik}A_{jl} l'_i l'_j l_k l_l + F^2\sum p_i B_{jkl} l'_i l'_j l_k l_l, \tag{15d}$$

$$(\boldsymbol{e}_{\parallel}\cdot\boldsymbol{p})^2(\boldsymbol{F}\cdot\Delta\boldsymbol{\alpha}\cdot\boldsymbol{F}) = F^2\sum p_i \Delta\alpha_{jkl} l_i l_j l_k l_l, \tag{15e}$$

$$(\boldsymbol{e}_{\perp}\cdot\boldsymbol{p})^2(\boldsymbol{F}\cdot\Delta\boldsymbol{\alpha}\cdot\boldsymbol{F}) = F^2\sum p_i \Delta\alpha_{jkl} l'_i l'_j l_k l_l, \tag{15f}$$

where $l_i$ is the direction cosine between the $i$th molecular axis and the $Z$ laboratory axis, $l'_i$ is the direction cosine between the $i$th molecular axis and an axis perpendicular to the $Z$ axis, $\chi$ is the experimentally variable angle between the electric vector of the polarized probe light and the $Z$ axis, $\boldsymbol{e}_{\parallel}$ and $\boldsymbol{e}_{\perp}$ are parallel and perpendicular to the $Z$ axis, respectively, $\theta$ is the angle between the $\Delta\boldsymbol{\mu}_A$ ($z$ axis) and the external field $\boldsymbol{F}$ ($Z$ axis), $\phi$ is the azimuthal angle in the molecular frame and $\psi$ is the azimuthal angle in the laboratory frame.

### 4.2. Model for the quantum yield failure function

When electric-field-dependent processes compete with the initial electron transfer are included, the quantum yield failure, $\Phi_1(\boldsymbol{F})$, of the primary step as the function of an applied external field is given as:

$$\Phi_1(\boldsymbol{F}) = k_Y(\boldsymbol{F})/[k_X(\boldsymbol{F}) + k_Y(\boldsymbol{F})]. \tag{16}$$

In Eq. (16), $k_X(\boldsymbol{F})$ is the rate constant for the initial electron transfer and $k_Y(\boldsymbol{F})$ is the sum of rate constants of all competing decay processes that contribute to QYF.

From Eq. (16), the relative quantum yield of the primary step can be expressed as the ratio of the bleach magnitudes measured with the field on and off.

$$\frac{1-\langle\Phi_1(\boldsymbol{F})\rangle}{1-\langle\Phi_1(0)\rangle} = \frac{\Delta\varepsilon(\nu,\boldsymbol{F})}{\Delta\varepsilon(\nu,0)} = 3\left\langle(\boldsymbol{e}\cdot\boldsymbol{p})^2\frac{1+k_Y(0)/k_X(0)}{1+k_Y(\boldsymbol{F})/k_X(\boldsymbol{F})}\right\rangle. \tag{17}$$

Since the $\chi$-dependent QYF data alone do not unambiguously constrain both difference dipole moments, an effective difference dipole, $\Delta\boldsymbol{\mu}_{QYF}$, is used to simplify Eq. (17). $\Delta\boldsymbol{\mu}_{QYF}$ could be the vector sum of several dipoles which are responsible for QYF. The angle $\zeta_{QYF}$ between $\Delta\boldsymbol{\mu}_{QYF}$ and transition dipole moment $\boldsymbol{p}$ is then defined as an effective or averaged angle.

Reaction kinetics in an electric field can be modeled using a cumulant expansion as the model function [12,17]. The rate constant is a function of the applied field and the relevant difference dipole moment:

$$k_Y(\boldsymbol{F})/k_X(\boldsymbol{F}) = \exp\left(\sum_{n=0}^{N}\left[C_n(\Delta\boldsymbol{\mu}_{QYF}\cdot\boldsymbol{F})^n\right]\right). \tag{18}$$

Since our focus is on $\Delta\boldsymbol{\mu}_{QYF}$, it is convenient to change the definition of the molecular axis so that $\Delta\boldsymbol{\mu}_{QYF}$ lies along the molecular $z$ axis. Eq. (17) is then given as:

$$\frac{1-\langle\Phi_1(\boldsymbol{F})\rangle}{1-\langle\Phi_1(0)\rangle} = \int_{-1}^{1}\frac{1-\Phi_1(\beta,\boldsymbol{F})}{1-\Phi_1(\beta,0)}\left[h_0 + h_1\cos^2(\beta)\right]\mathrm{d}\cos(\beta), \tag{19a}$$

where

$$h_0 = \sin^2(\zeta_{QYF})/4 + \cos^2(\zeta_{QYF})\,\sin^2(\chi)/2, \tag{19b}$$

$$h_1 = \left[\cos^2(\zeta_{QYF})/2 - \sin^2(\zeta_{QYF})/4\right]\left[\cos^2(\chi) - \sin^2(\chi)\right], \tag{19c}$$

and

$$\frac{1-\Phi_1(\beta, F)}{1-\Phi_1(\beta, 0)} = \frac{1+\exp(C_0)}{1+\exp\sum\left[C_n(\Delta\boldsymbol{\mu}_{QYF}\cdot\boldsymbol{F})^n\right]}, \tag{19d}$$

where $\beta$ is the angle between $\Delta\boldsymbol{\mu}_{QYF}$ ($z$ axis in the molecular frame) and the field $\boldsymbol{F}$ ($Z$ axis in the lab frame), and $\exp(C_0) = k_Y(0)/k_X(0)$.

### 4.3. Maximum entropy method

The dynamic Stark spectrum probes the distribution of $\Delta\boldsymbol{\mu}_A$ from those molecules which undergo QYF. The distribution obtained for $\Delta\boldsymbol{\mu}_A$ can be related to the distribution of $\Delta\boldsymbol{\mu}_{QYF}$, the quantity of interest (see Eq. (23) below). Introducing the orientation distribution function of $\Delta\boldsymbol{\mu}_A$ in electronic ground state, $g(\cos\theta)$, into Eq. (14) in place of the QYF term $\eta\Phi_1(\boldsymbol{F})$, the dynamic Stark term $\Delta\varepsilon^{DSS}(\nu, \boldsymbol{F})$ can be expressed as

$$\Delta\varepsilon^{DSS}(\nu, \boldsymbol{F}) = K\nu g(\cos\theta)\left[\langle(\boldsymbol{e}\cdot\boldsymbol{p})^2 S(\nu, \boldsymbol{F})\rangle - \langle(\boldsymbol{e}\cdot\boldsymbol{p}_0)^2 S(\nu, F=0)\rangle\right]. \tag{20}$$

Explicitly working out Eqs. (15a)–(15f):

$$\begin{aligned}\Delta\varepsilon^{S}(\nu, \boldsymbol{F}) = K\nu\sum_{i=1}^{N}\int_{-1}^{1} \mathrm{d}\cos(\theta)\; g(\cos\theta)\Big\{&\big(a_0 + a_1\cos(\theta) + a_2\cos^2(\theta)\\ &+ a_3\cos^3(\theta) + a_4\cos^4(\theta) + \left[(\nu-\nu_i)/\omega_i^2\right]\left[b_0 + b_2\cos^2(\theta)\right.\\ &\left.+ b_4\cos^4(\theta)\right]\big)\exp\Big\{-\left[\nu - \nu_i - |\Delta\boldsymbol{\mu}_A||\boldsymbol{F}|\cos(\theta)\right]^2/\omega_i^2\Big\}\\ &-\left[f_0 + f_2\cos^2(\theta)\right]\exp\left[-(\nu-\nu_i)^2/\omega_i^2\right]\Big\},\end{aligned} \tag{21}$$

where $a_n$ and $b_n$ are parameters related to the following molecular properties: $\boldsymbol{p}_0$ is the zero field transition dipole moment; **A** is the transition polarizability; **B** is the transition hyperpolarizability; $\Delta\boldsymbol{\alpha}$ is the difference polarizability; $\Delta\boldsymbol{\mu}_A$ is the difference dipole moment for the transition used to probe the dynamic Stark effect; and $\zeta_A$ is the angle between $\boldsymbol{p}$ and $\Delta\boldsymbol{\mu}_A$. $f_0$ and $f_2$ are geometric factors related to the angles $\zeta_A$ and $\chi$ (see Eqs. (22a) and (22b) below).

In Eq. (8), it was necessary to include the anisotropic absorption change due to the population which undergoes QYF, which is different from the isotropic absorption of the P band. In order to account for this anisotropy, the last term in Eq. (8) has the following form:

$$\eta\langle\Phi_1(\boldsymbol{F})\Delta\varepsilon_e(\nu, F=0)\rangle = \int_{-1}^{1} g(\cos\theta)\left[f_0 + f_2\cos^2(\theta)\right]\Delta\varepsilon_e(\nu, F=0)\,\mathrm{d}\cos(\theta), \tag{22}$$

where

$$f_0 = \sin^2(\zeta_A)\cos^2(\chi)/4 + \sin^2(\zeta_A)\sin^2(\chi)/8 + \cos^2(\zeta_A)\sin^2(\chi)/4,$$

$$f_2 = \left[\cos^2(\zeta_A)/2 - \sin^2(\zeta_A)/4\right]\cos^2(\chi) + \left[\sin^2(\zeta_A)/8 - \cos^2(\zeta_A)/4\right]\sin^2(\chi).$$

In order to obtain the distribution function $g(\cos\theta)$, we discretized the integration in Eq. (21) on an equally spaced grid along the variable $\cos\theta$, and use the maximum entropy method (MEM) to obtain the distribution

function $g(\cos\theta) = \sum g_n(\cos\theta)$, where $n$ is the number of grid points ($n = 128$ for our calculations). The dynamic Stark spectrum was then obtained from Eqs. (8), (21) and (22).

MEM has been frequently used to recover distribution functions [18,19]. Basically, an orientation distribution function $g(\cos\theta)$ is represented by a discrete set of data $g_n(\cos\theta)$. The amount of uncertainty involved in the specification of $g_n(\cos\theta)$ is measured by the Shannon–Jaynes entropy $S$. A single statistical constraint $C$, usually chi-squared, is used to measure the quality of the fit. MEM uses a Lagrangian function $Q = S - \lambda C$, and attempts to maximize the entropy $S$, subject to the constraint the quantity $C < C_{\text{aim}}$, where $C_{\text{aim}}$ is the statistical upper bound chi-squared. MEM yields the orientation distribution function having the smoothest features compatible with both the experimental data and the noise, and does not introduce spurious correlations into $g(\cos\theta)$. We refer to the extensive review by Skilling and Bryan for details.

MEM does not need a model function for the mechanism which causes the dynamic anisotropy distribution in the sample. However, it is imperative to have a good spectroscopic model for the static Stark effect. A new model for Stark effect based on the classic Liptay model, is presented in Eqs. (15)–(21). Imperfections in the static Stark model, used as a reference for the dynamic Stark spectrum, could lead to artificial structure in the distribution function of $\Delta\boldsymbol{\mu}_A$. Therefore it is necessary to obtain a pre-flash static Stark spectrum under identical conditions as the post-flash Stark effect. The parameters $a_n$ and $b_n$ in Eq. (21) were determined by fitting the static Stark spectrum, for an isotropic sample where $g(\cos\theta) = 1$. A baseline correction $B_0$ was included in Eq. (8) in order to take care of the errors due to laser fluctuation and imperfections in the deconvolution procedure. The $B_0$ were determined by minimizing the chi-squared for each distribution $g_n(\cos\theta)$. Technically, we decoupled the optimizing procedures of the $B_0$ from $g_n(\cos\theta)$ by alternating their calculation. This decoupling procedure avoids possible corruption of the entropy maximizing procedure and allows us to reduce the multi-dimensional MEM to a one-dimensional problem. For most cases, the physical properties, such as the baseline, the phase shift and the yield, have unique values in an experiment. It is not necessary to carry out a multi-dimensional MEM to find out that their distribution functions are $\delta$-functions.

## 5. Discussion

We employ two independent experimental methods to extract the orientation distribution function of the molecules which have undergone QYF in an applied electric field: (1) the field dependence of the quantum yield failure as a function of the experimental angle $\chi$; and (2) the dynamic Stark spectra observed during a $\mu$s time window.

### *5.1. Field and $\chi$ dependence of quantum yield failure*

Eq. (19d) is used to fit the QYF data as a function of electric field and experimental angle $\chi$ (Fig. 3). In order to achieve a good fit to the data, at least two cumulant terms were required. The angle $\zeta_{\text{QYF}}$ is determined to be $54° \pm 2°$ which is nearly equal to the magic angle. Examination of the three-dimensional structure of RCs [5] gives angles between the difference dipole moments, $\Delta\boldsymbol{\mu}_{P^+B^-}$ ($= \boldsymbol{\mu}_{P^+B^-} - \boldsymbol{\mu}_{iP}$) and $\Delta\boldsymbol{\mu}_{P^+H^-}$ ($= \boldsymbol{\mu}_{P^+H^-} - \boldsymbol{\mu}_{iP}$) of 49° and 59°, respectively. $\zeta_{\text{QYF}} = 54°$ is between these two angles. A possible explanation is that both difference dipole moments, and consequently both the $P^+B^-$ and $P^+H^-$ states, contribute to QYF, i.e., the effective difference dipole $\Delta\boldsymbol{\mu}_{\text{QYF}}$ is the vector sum of $\Delta\boldsymbol{\mu}_{P^+B^-}$ and $\Delta\boldsymbol{\mu}_{P^+H^-}$ with proper weighting factors (note that a contribution from charge-separated states with the special pair, i.e. $P^+P^-$, could also contribute to this effective $\Delta\boldsymbol{\mu}_{\text{QYF}}$). A more exotic possibility is that $\Delta\boldsymbol{\mu}_{\text{QYF}}$ is the average value of a transient difference dipole, for example of the $P^+H^-$ state whose magnitude and orientation may change with time. Although there is considerable evidence for a relaxation of the energy of the $P^+H^-$ state following its formation [21], these data provide no information on the time dependence of the dipole moment of this state. The result that the angle $\zeta_{\text{QYF}}$

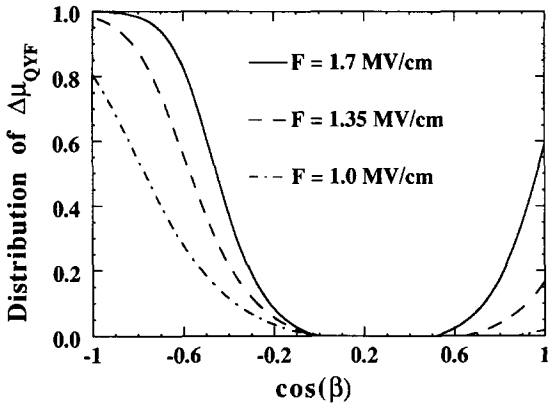


Fig. 8. Distributions of $\Delta\mu_{QYF}$ obtained from the data in Fig. 3 as a function of cos $\beta$ at several fields. Here, $\beta$ is the angle between $\Delta\mu_{QYF}$ and the field $F$.

is nearly the magic angle is clearly not sufficient information to make any distinction among the possible mechanisms.

The field-independent term $k_Y(F=0)/k_X(F=0)$ obtained from the fit is found to be 6%, compared to approximately 1% for native RCs [1]. This difference likely reflects the observation that the quantum yield of charge separation in the absence of a field is less than unity in dry PVA films [10].

The distribution function $\Delta\mu_{QYF}$ for those RCs which have returned to the ground state due to QYF is $\Phi_1(\beta, F)/\Phi_1(\beta, F=0)$ in Eq. (19d). The distribution shown in Fig. 8 was calculated as a function of the variable $\cos(\beta)$. In Fig. 8, when $\cos(\beta)$ is equal to 1 or $-1$, $\Delta\mu_{QYF}$ is parallel or anti-parallel, respectively, to the field $F$. One drawback of using measurements at a single wavelength is that the sign of the first-order term cannot be uniquely determined, i.e., the same fit to the QYF data is obtained when $C_1$ in Eq. (19d) is either positive or negative, with the consequence that the distribution function for $\Delta\mu_{QYF}$ can be reflected around $\cos(\beta)=0$. This ambiguity is not a problem in the dynamic Stark spectrum which contains information on the absolute orientation as the spectrum shifts. In anticipation of the analysis of the DSS below, we assign $C_1$ to be negative in order to facilitate comparison between the results of the two methods. In this case, the largest QYF occurs when $\cos(\beta)=-1$, that is, antiparallel to the field direction. When $F > 1.35$ MV/cm, QYF begins to occur also for those RCs which have the effective dipoles parallel with the applied field. At applied fields of 1.7 MV/cm, the QYF begins to saturate for those RCs which have their dipoles anti-parallel with the field and increases rapidly for those parallel with $F$. If it were possible to apply larger fields without dielectric breakdown, it should be possible to stop charge separation altogether, i.e., achieve a QYF approaching 100%.

### 5.2. Dynamic Stark spectra

The observation that the QYF is more than 50% at fields over 2.5 MV/cm [2] and that the distribution appears to be bimodal suggests that there are at least two mechanisms involved in the QYF. This could involve two independent dipoles or one dipole where both parallel and anti-parallel subpopulations contribute to QYF. If only one dipole is involved in QYF, the distribution of the subpopulations which undergo field-induced QYF will be bimodal and symmetrical around $\cos(\theta)=0$, where the field and the dipole are perpendicular to each other. If two dipoles are important, the distribution is likely to be unsymmetrical.

The MEM method was used to fit the dynamic Stark spectra (Fig. 6B) in order to generate the orientation distribution functions of $\Delta\mu_A$ at three different applied fields, as shown in Fig. 9. The distribution is unsymmetrical around $\cos\theta=0$ with a clear peak at $\cos\theta\simeq 0.45$ and a broad lump at $\cos\theta\simeq -0.8$. This suggests at least two different difference dipole moments are responsible for QYF.

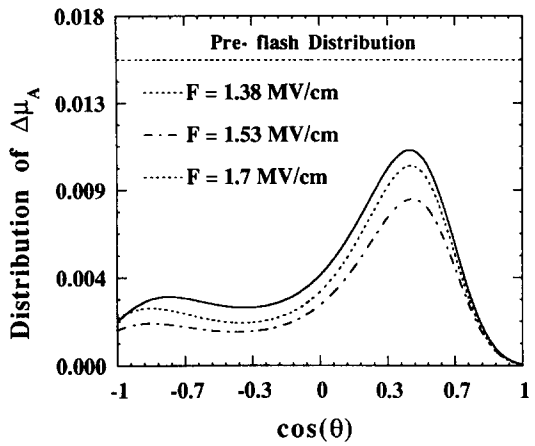


Fig. 9. The MEM distributions of $\Delta\mu_A$ as a function of $\cos\theta$ at $F = 1.38$ MV/cm (long-short dashed line), $F = 1.53$ MV/cm (dashed line), and $F = 1.70$ MV/cm (solid line). The flat dashed line at the top of the plot is the pre-flash distribution of $\Delta\mu_A$ ($\theta$ is the angle between $\Delta\mu_A$ and $F$).

To compare results from the model function and MEM approaches, the distribution function of $\Delta\mu_A$ at 1.53 MV/cm in Fig. 9 was deconvolved into two distribution functions for two effective difference dipole moments, denoted $\Delta\mu_{QYF1}$ and $\Delta\mu_{QYF2}$. The larger component in the distribution function for $\Delta\mu_A$ peaked at $\cos\theta \simeq 0.45$ in Fig. 9 is associated with $\Delta\mu_{QYF1}$, and the other component peaked at $\cos\theta \simeq -0.8$ is associated with $\Delta\mu_{QYF2}$, and the separate components are depicted in Fig. 10B. $\Delta\mu_{QYF1}$ and $\Delta\mu_{QYF2}$ make angles $\alpha$ and $\gamma$ relative to $\Delta\mu_A$ (see Fig. 7). Since we do not know the angles $\alpha$ and $\gamma$, distributions were calculated for several possible angles by using the following relationship for $\Delta\mu_{QYF1}$:

$$\cos(\beta) = \sin(\alpha)\cos(\psi)\sin(\theta) + \cos(\theta)\cos(\alpha), \tag{23}$$

where $\beta$ is the angle between $\Delta\mu_{QYF1}$ or $\Delta\mu_{QYF2}$ and the field $F$, and $\theta$ is the angle between $\Delta\mu_A$ and the field $F$. For $\Delta\mu_{QYF2}$, the angle $\alpha$ is replaced by $\gamma$ in Eq. (23). Since the distribution function for angles $\alpha$ and $\gamma$ are mirror images of the angles $(180° - \alpha)$ and $(180° - \gamma)$, respectively, only angles larger than 90° are presented in Figs. 10A and 10B. The angles which give the sharpest features at $\cos\theta = -1$ are $\alpha = 120° \pm 10°$ ($\Delta\mu_{QYF1}$) and $\gamma = 30° \pm 10°$ ($\Delta\mu_{QYF2}$), and the angles which give the sharpest feature at $\cos\theta = 1$ are $\alpha = 60° \pm 10°$ ($\Delta\mu_{QYF1}$) and $\gamma = 150° \pm 10°$ ($\Delta\mu_{QYF2}$).

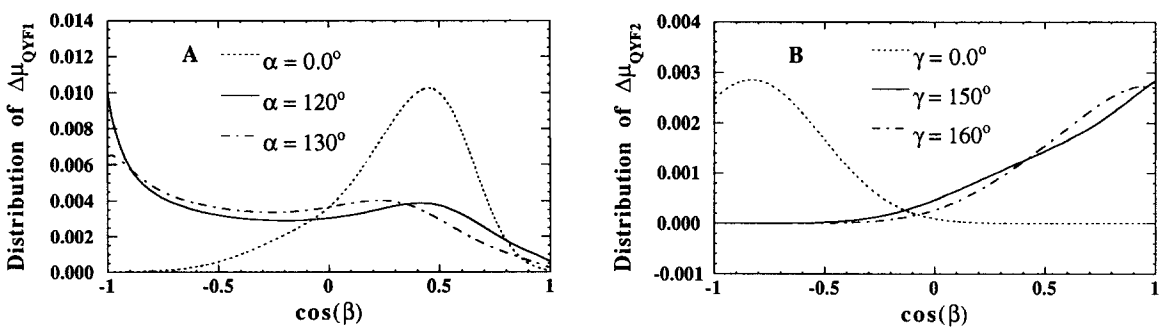


Fig. 10. (A) The distribution functions of $\Delta\mu_{QYF1}$ as a function of $\alpha$, the angle between $\Delta\mu_{QYF1}$ and $\Delta\mu_A$: $\alpha = 0°$ (dotted lines); $\alpha = 120°$ (solid line) and $\alpha = 130°$ (dash-dotted lines); (B) The distribution functions of $\Delta\mu_{QYF2}$ as a function of $\gamma$, the angle between $\Delta\mu_{QYF2}$ and $\Delta\mu_A$: $\gamma = 0°$ (dotted lines); $\gamma = 150°$ (solid line), and $\gamma = 160°$ (dash-dotted lines). Here $\beta$ is the angle between $\Delta\mu_{QYF1}$ or $\Delta\mu_{QYF2}$ and the applied field $F$.

Table 1
Identity of states and relevant angles for two possible orientations of $\Delta\mu_A$ consistent with the distributions of orientational subpopulations obtained from the electric field dependence of the quantum yield and dynamic Stark effect data

| Direction of $\Delta\mu_A$ [a] | Angle between $\Delta\mu_A$ and difference dipole moments | | | Identities of dipoles | | Angle between $\Delta\mu_{QYF1}$ and $\Delta\mu_{QYF2}$ |
|---|---|---|---|---|---|---|
| | $\Delta\mu_{P_M^+P_L^-}$ | $\Delta\mu_{P^+B^-}$ | $\Delta\mu_{P^+H^-}$ | $\Delta\mu_{QYF1}$ | $\Delta\mu_{QYF2}$ | |
| 1 | 17 | 99 | 115 | $P^+H^-$ | $P^+B^-$ | 35 |
| 2 | 80 | 155 | 120 | $P^+H^-$ | $P^+P^-$ [b] | 70 |

[a] The angle between $\Delta\mu_A$ and the transition moment of P is 45° in both cases since both of these possible directions lie on the cone of possible directions determined from the isotropic Stark effect [27]. The coordinates for *Rps. viridis* [5] $(X, Y, Z)$ giving possible directions of $\Delta\mu_A$ are: direction 1 = (−0.591, 0.341, −0.371) and direction 2 = (−0.446, 0.558, 0.687).
[b] The state $P^+P^-$ could be either $P_M^+P_L^-$ or $P_L^+P_M^-$ since these are separated by 180°. The angle $\gamma$ between $\Delta\mu_{QYF2}$ and $\Delta\mu_A$ could equally well be $180°-\gamma$ (see text). The remaining angles in the Table are given for $P_M^+P_L^-$ and can be corrected similarly for the state $P_L^+P_M^-$.

A physical interpretation of the observed QYF requires that $\Delta\mu_{QYF1}$ and $\Delta\mu_{QYF2}$ are related to one or more of the difference dipole moments, $\Delta\mu_{P^+H^-}$, $\Delta\mu_{P^+B^-}$, and $\Delta\mu_{P^+P^-}$, associated with charge-separated state $P^+H^-$, $P^+B^-$, and $P^+P^-$, respectively. The data rule out the possibility that $\Delta\mu_{QYF}$ is due solely to $\Delta\mu_{P^+P^-}$. If $\Delta\mu_{P^+P^-}$ alone were identical to $\Delta\mu_{QYF}$, then the distribution of $\Delta\mu_A$ would peak at the two extrema ($\cos\theta = \pm 1$) in Fig. 9, making the reasonable assumption that $\Delta\mu_A$ and $\Delta\mu_{P^+P^-}$ are nearly colinear. From inspection of the *R. viridis* RC crystal structure [5], the angle between the transition dipole moment $p$ and $\Delta\mu_{P^+H^-}$ is about 59° (or 121°), and the angle between $p$ and $\Delta\mu_{P^+B^-}$ is about 49° (or 131°), giving an angle between $\Delta\mu_{P^+H^-}$ and $\Delta\mu_{P^+B^-}$ of about 35°. In order to go further with this type of analysis, one needs to know the absolute (molecular axis fixed) direction of $\Delta\mu_A$. Some information on this direction can be obtained by measuring the spectral bandshift on the P $Q_y$ electronic transition at 870 nm in the presence of a charge on $Q_A^-$ [22]. In this case the absolute location of the charge producing the shift is known, and it is possible to extract four directions of $\Delta\mu_A$ which are consistent with the (small) observed shift. This approach contains too many uncertainties to be useful at this time, although ultimately an accurate absolute direction for $\Delta\mu_A$ will be available.

An alternative approach is to examine the directions of $\Delta\mu_A$ which are consistent with the angles found for $\alpha$ and $\gamma$ from the distributions of orientational subpopulations. These two directions, denoted 1 and 2, are given in Table 1. Interestingly, either of these possible directions for $\Delta\mu_A$ identifies $\Delta\mu_{QYF1}$ with the $P^+H^-$ state. For orientational subpopulations where the $P^+H^-$ dipole opposes the field direction, the $P^+H^-$ state is raised in energy. The free energy of the $P^+H^-$ state is estimated to be about 2000 $cm^{-1}$ below that of the $^1P$ state [23]. An increase in the free energy of $P^+H^-$ will decrease the driving force of $^1P \rightarrow P^+H^-$ electron transfer, and should lead to a reduction in the quantum yield if the reaction is activationless, as is often suggested based on the observed independence of the rate on temperature [24]. Independent evidence for the consequences of raising the energy of $P^+H^-$ can be found in the slower kinetics of charge separation and enhanced recombination rate of the mutant (M)L214H, where a BChl (denoted $\beta$) replaces $H_L$, shifting the $P^+\beta^-$ energy closer to that of $^1P$ [25].

The identification of $\Delta\mu_{QYF2}$ is less clear. Direction 2 for $\Delta\mu_A$ (Table 1) is nearly orthogonal to the $P^+P^-$ direction. This would not be in accord with the notion that the difference dipole which gives rise to the isotropic Stark effect for P is mixing with states such as $P^+P^-$. By contrast, Direction 1 is consistent with $\Delta\mu_A$ having a large contribution of mixing with the $P^+P^-$ state. As stated above, the data exclude the possibility that $P^+P^-$ is solely responsible for the observed reduction in quantum yield; however, it is possible that it plays a role in the competition between forward electron transfer to $P^+H^-$ and internal converstion to the ground state. A possibly related example is the heterodimer mutant (M)H202L whose lowest electronic state(s) appear to be much more dipolar than the homodimer [26] and where the quantum yield of charge separation is greatly reduced due to

slower charge separation and enhanced internal conversion. An analogous situation may apply for those orientational subpopulations where the $P^+P^-$ energy is aligned with the externally applied electric field. Finally we note that the angle between $\Delta\mu_{P^+P^-}$ and $\Delta\mu_{P^+H^-}$ estimated from the X-ray structure is about 70°. The orientation averaged, dipole-weighted vector sum of the two difference dipoles $\Delta\mu_A$ (approximately 5D) and $\Delta\mu_{P^+H^-}$ (approximately 80D) will alter the effective direction of $\Delta\mu_{P^+H^-}$ from 59° to an angle closer to the magic angle, in agreement with the observation that the field dependence of QYF is independent of the angle used to probe QYF.

In conclusion, the dynamic Stark effect data require contributions from at least two dipoles to explain QYF. Although the detailed identification is still subject to refinement, the data are consistent with a change in the competition between internal conversion and charge separation as the root cause of QYF, a phenomenon which is well documented in single-site mutants. Future insight into the mechanism of QYF will require a direct measurement of the effect of the field on the $^1P$ lifetime, the use of much shorter pulsed fields, a combination of mutations and electric fields, and information on the absolute direction of $\Delta\mu_A$. Experiments to address each facet are currently in progress.

## Acknowledgement

This work was supported in part by a grant from the NSF Biophysics Program.

## References

[1] C.A. Wraight and R.K. Clayton, Biochem. Biophys. Acta 333 (1973) 246.
[2] K. Lao, S. Franzen, R.J. Stanley, D.G. Lambright and S.G. Boxer, J. Phys. Chem. 97 (1993) 13165.
[3] A. Ogrodnik, T. Langenbacher, G. Bieser, J. Siegl, U. Eberl, M. Volk and M. Michel-Beyerle, Chem. Phys. Letters 198 (1992) 653; J. Phys. Chem. 97 (1993) 9831.
[4] S.G. Boxer, in: Methods in photosynthesis research, eds. A. Hoff and J. Amesz, in press.
[5] J. Deisenhofer, O. Epp, K. Miki, R. Huber and H. Michel, Nature 318 (1985) 618.
[6] S.G. Boxer, R. Goldstein, D.J. Lockhart, T. Middendorf and L.J. Takiff, J. Phys. Chem. 93 (1989) 8280.
[7] D.J. Lockhart, R. Goldstein and S.G. Boxer, J. Chem. Phys. 89 (1988) 1408.
[8] D.J. Lockhart, C. Kirmaier, D. Holten and S.G. Boxer, J. Phys. Chem. 94 (1991) 6987.
[9] W. Holzapfel, U. Finkele, W. Kaiser, D. Oesterhelt, H. Scheer, H. Stilz and W. Zinth, Proc. Natl. Acad. Sci. US 87 (1989) 5168.
[10] D.J. Lockhart, S. Hammes, S. Franzen and S.G. Boxer, J. Phys. Chem. 95 (1991) 2217.
[11] S. Franzen and S.G. Boxer, J. Phys. Chem. 97 (1993) 6304.
[12] S. Franzen, R. Goldstein and S.G. Boxer, J. Phys. Chem. 94 (1990) 5135.
[13] D.J. Lockhart and S.G. Boxer, Proc. Natl. Acad. Sci. US 85 (1988) 107.
[14] S.G. Boxer, C.E.D. Chidsey and M.G. Roelofs, Proc. Natl. Acad. Sci. US 79 (1982) 4632.
[15] S.G. Boxer, in: The photosynthetic reaction center, Vol. 2, eds. J. Deisenhofer and J.R. Norris (Academic Press, San Diego, 1993) p. 179.
[16] W. Liptay, in: Excited states, Vol. 1, ed. E.C. Lim (Academic Press, New York, 1974) p. 129.
[17] S. Franzen, K. Lao and S.G. Boxer, Chem. Phys. Letters 197 (1992) 380.
[18] J. Skilling and R. Bryan, Mon. Not. Roy. Astron. Soc. 211 (1984) 111.
[19] J. Skilling, in: Maximum entropy and Bayesian method, ed. J. Skilling (Kluwer, Dordrecht, 1989).
[20] N.W. Woodbury and W.W. Parson, Biochim. Biophys. Acta 767 (1984) 345.
[21] R. Goldstein and S.G. Boxer, Biochim. Biophys. Acta 977 (1989) 78, 87.
[22] M. Steffen, Ph.D. Thesis, Stanford University, 1994.
[23] R.A. Goldstein, L. Takiff and S.G. Boxer, Biochim. Biophys. Acta 934 (1988) 253.
[24] G.R. Fleming, J.-L. Martin and J. Breton, Nature 333 (1988) 190.
[25] C. Kirmaier, D. Gaul, R. DeBey, D. Holten and C. Schenck, Science 251 (1991) 922.
[26] S. Hammes, L. Mazzola, S.G. Boxer, D. Gaul and C. Schenck, Proc. Natl. Acad. Sci. USA 87 (1990) 5682.
[27] T.R. Middendorf, L.T. Mazzola, K. Lao, M.A. Steffen and S.G. Boxer, Biochim. Biophys. Acta 1144 (1993) 223.